Shap. Mem. Superelasticity (2016) 2:18–28
DOI 10.1007/s40830-016-0057-0

SPECIAL ISSUE: RESEARCH ON BIOMEDICAL SHAPE MEMORY ALLOYS, INVITED PAPER

# Deformation Mechanisms and Biocompatibility of the Superelastic Ti–23Nb–0.7Ta–2Zr–0.5N Alloy

**P. Castany[1] · D. M. Gordin[1] · S. I. Drob[2] · C. Vasilescu[2] · V. Mitran[3] · A. Cimpean[3] · T. Gloriant[1]**

Published online: 26 February 2016


**Abstract** In this study, we have synthesized a new Ti–23Nb–0.7Ta–2Zr–0.5N alloy composition with the aim to obtain useful mechanical properties to be used in medicine such as high strength, good superelastic property, low modulus, and large ductility. Thus, mechanical properties including superelasticity and plasticity were investigated in relation with the different deformation mechanisms observed (stress-induced martensitic transformation, twinning and dislocation slip). On the other hand, the corrosion resistance in simulated body fluid (Ringer solution) and the in vitro cell behavior (MG63 human osteoblasts) of such biomedical alloy were also evaluated in order to assess its biocompatibility.

**Keywords** Titanium · Superelasticity · Plastic deformation · Biocorrosion · Cytocompatibility

## Introduction

Alloys possessing shape memory or superelastic behavior are of great interest for biomedical functional devices such as stents, osteosynthesis staples, and orthodontic arch wires. The alloys commonly used for such devices belong to the NiTi family (e.g., Nitinol) due to their exceptional shape memory and superelastic properties. However, hypersensitivity and toxicity of nickel remain as the problems in many clinical cases and the use of nickel must be avoided [1]. Consequently, nickel-free titanium-based alloys composed only of non-cytotoxic alloying elements such as Nb, Ta, and Zr are now widely studied [2–4]. The reason for this interest is due to the fact that, depending to the chemical composition, metastable β titanium-based alloys can be mechanically unstable. Consequently, they can also exhibit shape memory effect and superelastic behavior. Indeed, a reversible martensitic transformation between the parent β-phase (austenite) and the α″-phase (martensite) formed is observed in such alloys [5, 6]. Superelastic (or pseudoelastic) behavior is obtained when the quenched microstructure is composed of the β-metastable phase at room temperature. In this case, a stress-induced martensitic transformation (β into α″) can directly occur under mechanical stimulation and large elastic recovery can be obtained due to the fact that this transformation is fully reversible once the mechanical stress is released. On the other hand, a much lower elastic modulus is obtained with such superelastic alloys by comparison with the typical Ti–6Al–4V alloy currently used as prosthetic material [3–6]. Low rigidity is known to be very beneficial to avoid the stress-shielding phenomenon which can cause the premature loss of hip prostheses or dental implants for example [2, 4, 7]. Numerous works carried out on this kind of alloy have focused on alloys belonging to the binary Ti–Nb system. Unfortunately, the superelastic property observed is far less than that of NiTi and does not exceed 2 % of elastic recovery at best [3–6]. However, it was shown that addition of a third or a fourth element such as Zr, Al, or Sn improves the elastic recovery and about

✉ T. Gloriant
Thierry.Gloriant@insa-rennes.fr

[1] Institut des Sciences Chimiques de Rennes, UMR CNRS 6226, INSA Rennes, 20 Avenue des Buttes de Coësmes, 35708 Rennes, France

[2] Institute of Physical Chemistry "Ilie Murgulescu" of Romanian Academy, Spl. Independentei 202, 060021 Bucharest, Romania

[3] Department of Biochemistry and Molecular Biology, University of Bucharest, 91-95 Spl. Independentei, 050095 Bucharest, Romania

3 % of elastic recovery can be reached in some cases [8, 9]. Furthermore, addition of interstitial alloying elements (O, N) was also observed to be beneficial to enhance significantly both the superelasticity and the mechanical strength [10–12].

In this study, we have synthesized a new Ti–23Nb–0.7Ta–2Zr–0.5N alloy composition (at.%), which was inspired from the multifunctional β-type Ti–23Nb–0.7Ta–2Zr–1.2O alloy composition, called "gum metal" [13]. The difference is that we have replaced the oxygen by nitrogen in the original composition. It is worth noting that our first intention was to add 1 at.% of N but with such amount of N, the formation of nitride could not be avoided probably due the fact that the solubility of N in the beta solid solution is lower than the O one. Thus, the main objective is to show if the claimed "super" mechanical properties of the "gum metal" alloy are still obtained by this alternative alloy composition and to investigate its deformation mechanisms. Indeed, in addition to a superelastic behavior, various mechanisms of plastic deformation can be activated in Ti–Nb based alloys depending on the composition and thus on the stability of the beta phase. It was reported that the plastic deformation can be accommodated by both dislocations slip and twinning in such alloys [14–16]. To investigate the deformation mechanisms in the present study, uniaxial tensile tests were performed on normalized specimens. Then, electron backscattered diffraction (EBSD) and transmission electronic microscopy (TEM) observations were done after deformation to determine precisely the mechanisms of the plastic deformation. In situ tensile experiments in TEM were also carried out. As the Ti–23Nb–0.7Ta–2Zr–0.5N alloy can be of great interest for biomedical applications, its biocorrosion behavior in simulated body fluid and its cytocompatibility using in vitro tests performed on human MG63 osteoblasts were also evaluated in the present study.

## Materials and Methods

### Alloy Synthesis and Sample Preparation

As titanium, zirconium, tantalum, and niobium have melting points and densities which are very different, the synthesis of the Ti–23Nb–0.7Ta–2Zr–0.5N alloy composition (at.%) was realized by cold crucible levitation melting (CCLM) technique under high vacuum, using a high-frequency magnetic induction generator heating system. With this method, the high-frequency magnetic field is used to stir the liquid, which is useful in ensuring that alloying elements are fully mixed into the melt without contamination thanks to the restricting contact points between the melt and the cold crucible. The added elements are pure solid metals, except nitrogen, which was introduced through titanium nitride (TiN) powder. After a homogenization treatment at 950 °C for 16 h, the ingot was cold rolled at room temperature to reach 1 mm in thickness that corresponds to 90 % of reduction in thickness.

From the sheet, tensile test samples were machined to obtain normalized shapes: 3 mm width, 1 mm in thickness and a gage length of 15 mm. On the other hand, disk-shaped samples (diameter: 13 mm, thickness: 1 mm) were cut for the biological and the electrochemical tests.

Then, all samples were solution treated under high vacuum at 850 °C for 0.5 h in the beta-phase field and water quenched. The aim of this treatment is to restore a fully recrystallized beta microstructure from the cold rolled state. Finally, all samples were mechanically polished on silicon carbide abrasive papers (up to 4000 grit) and then ultrasonically cleaned in acetone, thoroughly washed with ethanol, and dried in air.

### Microstructural and Mechanical Characterization Methods

In this work, microstructures before and after deformation were observed by optical microscopy (OM). For the OM observations, samples were mechanically "mirror" polished using a colloidal silica suspension (particles size: 50 nm) and etched in a 5 % HF, 5 % $HNO_3$, 90 % $H_2O$ solution. Characterizations by electron backscattered diffraction (EBSD) on deformed samples were also conducted in a scanning electron microscope (Jeol JSM 6400, SEM) equipped with a TSL EBSD system. TEM observations were performed on a Jeol 2010 working with an accelerating voltage of 200 kV. TEM samples were thinned down with a Struers twin-jet electropolishing system using a 4 % perchloric acid solution in methanol. A video-rate SIS CCD camera and a Gatan straining holder were used for in situ straining experiments.

Tensile tests were carried out at room temperature (Instron machine, strain rate: $10^{-4}$ $s^{-1}$). All tensile tests were performed with the tensile direction parallel to the rolling direction. In this study, cyclic tensile tests consisting of applying 0.5 % strain increments (each followed by a stress release) were specifically carried out in order to characterize the superelastic property. An extensometer was used to precisely measure the deformation of the samples.

### Electrochemical and Corrosion Behavior Testing

The electrochemical behavior of the Ti–23Nb–0.7Ta–2Zr–0.5N alloy in simulated body fluid (SBF) was studied by the potentiodynamic cyclic and linear polarization tests. Commercially pure Ti (CP-Ti grade 2 provided by

Goodfellow) was also used as reference in this study. The SBF chosen was the Ringer solution at a neutral pH of about 7.4, which is the normal pH of the human biofluid [17]. The composition of Ringer solution was (g/L): NaCl—6.8; KCl—0.4; $CaCl_2$—0.2; $MgSO_4{\cdot}7H_2O$—0.2048; $NaH_2PO_4{\cdot}H_2O$—0.1438; $NaHCO_3$—1.1; glucose—1. The electrochemical experiments took place in a glass electrochemical cell. Disks of Ti–23Nb–0.7Ta–2Zr–0.5N alloy and CP-Ti were used as the working electrodes connected with saturated calomel electrode (SCE) by a Luggin–Haber capillary; auxiliary electrode was a platinum plate. The working electrodes were ultrasonically degreased in acetone and bidistilled water for every 30 min and dried in air.

The measurements were performed with Voltalab 80 equipment. Cyclic potentiodynamic polarization curves were recorded starting from a value of about 300 mV more negative than the open circuit potential and continue to positive direction till +1000 mV (versus SCE) with a scan rate of 1 mV/s. The main electrochemical parameters were determined: $E_{corr}$: corrosion potential as zero current potential; $E_p$: passivation potential where the current density becomes constant; $|E_{corr} - E_p|$: tendency to passivation with low values characterizes a strong, easy passivation; $i_p$: passive current density representing the corrosion resistance of the passive layer.

Linear potentiodynamic polarization was carried out for ±50 mV around the open circuit potential at a scan rate of 0.1 mV. Tafel representations were adjusted by Volta-Master 4 program and the main corrosion parameters were directly supplied: $i_{corr}$: corrosion current density; $V_{corr}$: corrosion rate; $R_p$: polarization resistance. Also, using the corrosion rate, we calculated the ion release rate representing the total quantity of ions released into the surrounding biofluid: Ion release rate $= 1.016 \times V_{corr} \times 102$, where the ion release rate is expressed in ng/cm$^2$ and $V_{corr}$ in μm/year [18–20].

Three samples were used for every experiment and the results reproducibility was very good.

### In Vitro Assessment of Osteoblast Behavior

The cell culture model used in cytocompatibility studies was represented by a human osteoblast-like cell line, MG63 (American Type Culture Collection, CRL-1427). These cells were seeded onto the tested Ti–23Nb–0.7Ta–2Zr–0.5N and CP-Ti materials at an initial density of $5 \times 103$ cells cm$^{-2}$ in Dulbecco's modified eagle medium (DMEM) containing 1 ‰ glucose, supplemented with 10 % heat-inactivated fetal bovine serum and 1 % (v/v) penicillin/streptomycin (10,000 units mL$^{-1}$ penicillin and 10 mg mL$^{-1}$ streptomycin). Previously to in vitro tests, the titanium-based samples were sterilized by immersion in 70 % ethanol, washed with sterile-filtered Milli-Q water, maintained under ultraviolet light in a sterile tissue culture hood for 1 h on each side, and conditioned in culture medium. The cells were maintained in contact with these samples in a humidified atmosphere of 5 % $CO_2$ at 37 °C for specific points in time. The medium was exchanged every 2nd day. All experiments have been done in triplicate.

Viability of MG63 osteoblasts cells was evaluated by combining a cytotoxicity test consisting in the assessment of lactate dehydrogenase (LDH) released into the culture medium and MTT [3-(4, 5-dimethyl thiazol-2-yl) 2,5-diphenyltetrazolium bromide] colorimetric study which also represents a useful indication of cell proliferation rates. LDH assay was carried out by using a cytotoxicity detection kit (Tox-7, Sigma-Aldrich) according to the manufacturer's protocol. Absorbance was evaluated at 490 nm using a microplate reader (Thermo Scientific Appliskan). MTT assay has been performed as previously reported [21]. Both assays were conducted at 1, 3, and 5 days after seeding.

Statistical analysis was performed with GraphPad Prism software using one-way ANOVA with Bonferroni's multiple comparison tests. Triplicate samples were used in LDH and MTT experiments to ensure the reproducibility of the results. The data are presented as mean ± SD (standard deviation). The $p$ values $<0.05$ were considered to be statistically significant.

## Results and Discussion

### Superelastic Deformation

Figure 1 shows an optical micrograph displaying the typical microstructure of the solution-treated and quenched Ti–23Nb–0.7Ta–2Zr–0.5N alloy. As it can be observed, the microstructure consists of a fully equiaxed β-grain

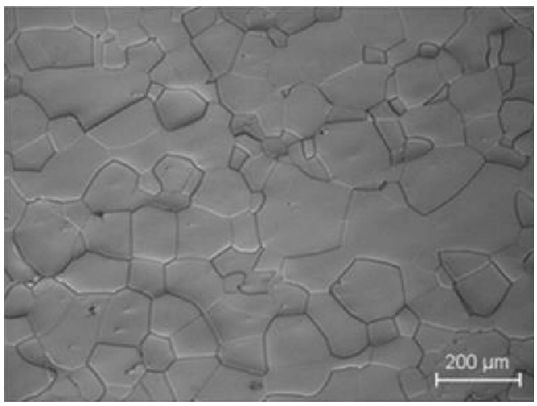


**Fig. 1** Optical micrograph of the Ti–23Nb–0.7Ta–2Zr–0.5N alloy

microstructure with a grain dimension varying between a few tens to a few hundreds of micrometers.

In Fig. 2, it is reported that a typical engineering stress–strain curve until rupture is obtained from the Ti–23Nb–0.7Ta–2Zr–0.5N alloy by tensile test. On the other hand, the cyclic tensile curve between 0 and 4 % of strain is also presented in this figure (center part) in order to characterize properly the superelastic behavior of such alloy. It is worth noting the excellent repeatability of the mechanical experiments because very similar strain–stress tensile curves were obtained for the five tests carried out. It can be clearly observed that the nonlinearity of the elastic domain and the presence of hysteresis loop between each loading–unloading cycle, which is a characteristic of a superelastic behavior. From this curve, a relatively high elastic recovery at about 2.2 % was evaluated and a low incipient Young's modulus measured at 50 GPa was found, which is very low compared to that obtained from classical titanium alloys currently used in medicine (110 GPa for Ti–6Al–4 V) and closer to the one that corresponds to the cortical bone (20–30 GPa). These good properties are due to the fact that a stress-induced martensitic transformation occurred in this alloy.

Figure 3 shows a typical bright field TEM image (a) and the corresponding electron diffraction pattern (b) of the Ti–23Nb–0.7Ta–2Zr–0.5N alloy microstructure after being deformed up to 4 % strain. In the bright field image, the typical needle-like morphology of the $\alpha''$ martensitic phase is observed confirming that double yielding observed on the tensile curve for this alloy composition is definitely related to the stress-induced $\alpha''$ martensitic transformation. The electron diffraction pattern exhibits typical diffraction spots related to the presence of both body-centered cubic β matrix and C-centered orthorhombic $\alpha''$ martensite needles. From the electron diffraction pattern, the orientation relationships between β and $\alpha''$ were found to be: $\langle 100\rangle_\beta$//$[100]_{\alpha''}$ and $\{110\}_\beta$//$(001)_{\alpha''}$ and the habit planes were found to be close to $\{112\}_\beta$ and $\{113\}_{\alpha''}$. These orientation relationships are consistent with those found in the literature [22]. In the present alloy composition, the lattice parameters were measured to be: $a_\beta = 0.327$ nm, $a_{\alpha''} = 0.317$ nm, $b_{\alpha''} = 0.481$ nm and $c_{\alpha''} = 0.463$ nm. These values are in good accordance with those obtained from similar Ti–Nb-based alloy compositions [23, 24].

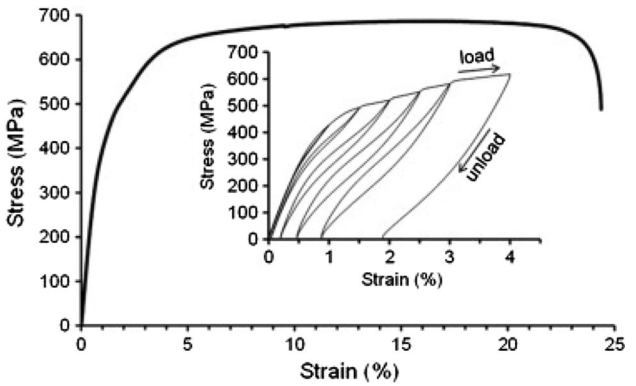


**Fig. 2** Engineering stress–strain tensile curves until rupture and loading/unloading cycles between 0 and 4 % of strain (*center part*) for the Ti–23Nb–0.7Ta–2Zr–0.5N alloy

As observed in the literature [20], the stress-induced martensitic transformation is accompanied by a significant reduction of the Young's modulus and a large strain recovery. On the other hand, the tensile curve of the Ti–23Nb–0.7Ta–2Zr–0.5N alloy shows both high yield strength at around 600 MPa and ultimate tensile strength at about 700 MPa, which are almost twice higher in comparison with the binary Ti–26Nb alloy reported from the literature [3]. This strengthening is due to the fact that nitrogen, as interstitial element, is well known to involve a solid-solution hardening effect in alloys. In addition, it can be noticed that nitrogen addition leads also to a higher superelasticity (almost by 1.5 higher) in comparison with the Ti–Nb or Ti–Nb–Ta alloys reported from the literature [3, 5, 6]. In fact, it was recently established [10] that the stability of superelasticity was improved by the addition of N due to the increase of the critical stress for slip.

## Plastic Deformation Mechanisms

Figure 4 shows an optical micrograph displaying the microstructure of the Ti–23Nb–0.7Ta–2Zr–0.5N alloy after being deformed up to 10 % strain. The formation of numerous large deformation bands of a few micrometers in thickness can be observed. In β-type titanium-based alloys, plastic deformation is known to be accommodated by dislocation glide and, in some cases, by twinning formation. In the present case, most of the β grains presented large deformation bands after deformation such as in Fig. 4. According to the literature of β titanium alloys, such large deformation bands are probably twins instead of dislocation slip bands that are commonly thinner [11, 14, 16], as confirmed from the EBSD analysis presented in Fig. 5. It was reported that two twinning systems are commonly observed in metastable β titanium alloys: {332} ⟨113⟩ and {112} ⟨111⟩ [14, 16].

In the present study, the twinning formation in the Ti–23Nb–0.7Ta–2Zr–0.5N alloy is illustrated from EBSD cartographies presented in Fig. 5. Fig. 5a shows several grains containing deformation bands with strong misorientation with the parent grain. Two misorientation profiles along lines denoted AB and BC crossing deformation bands are provided as examples and prove that deformation bands observed by optical microscopy are twins. For each grain, the orientations of the parent crystal and twins were

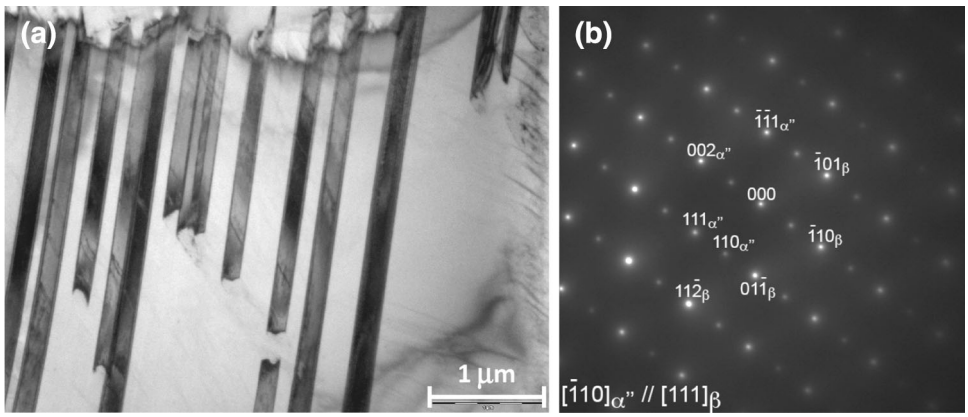


**Fig. 3** **a** Bright field TEM image of $\alpha''$ martensitic phase observed in the deformed Ti–23Nb–0.7Ta–2Zr–0.5N alloy and **b** corresponding electron diffraction pattern

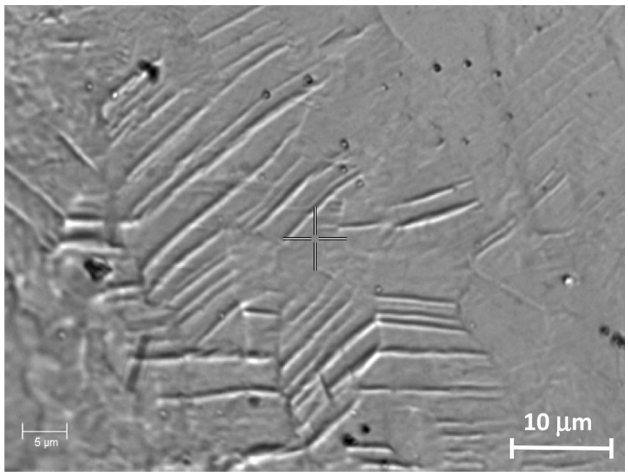


**Fig. 4** Optical micrograph of the Ti–23Nb–0.7Ta–2Zr–0.5N alloy after being deformed

determined by the Euler angles. The twinning system was then characterized from the existence of poles belonging to the parent crystal and the twin. To ensure statistics, about twenty grains on several zones of the tensile specimen were analyzed. By way of illustration, two grains denoted G1 in Fig. 5b and G2 in Fig. 5c and their twins, respectively, denoted T1 and T2 were located on the EBSD cartography as presented in Fig. 5a. In G1, the pole figures of {332} and {113} poles show common poles between the parent grain and the twin (circled on pole figures). The twinning system activated in G1 is then {332} ⟨113⟩. Conversely, analysis of pole figures in G2 shows common {112} and {111} poles between the twin and the parent grain. In G2, the other twinning system {112} ⟨111⟩ is then activated. It was checked that the coefficient site lattice (CSL) of the {112} ⟨111⟩ twin is a Σ3 boundary, which corresponds to a misorientation of 60° around ⟨111⟩. When the twinning system is {332} ⟨113⟩, the CSL boundary is Σ11, which corresponds to a misorientation of 50.57° around ⟨110⟩ (see Fig. 5a for examples). Thus, the plastic deformation of the present superelastic alloys is largely accommodated by twinning and the two {332} ⟨113⟩ and {112} ⟨111⟩ twinning systems were observed to be activated.

In order to characterize dislocation slip activity, in situ tensile tests were performed in TEM. During in situ experiments, dislocations were observed to nucleate first at grain boundaries and then propagate within the grains, as already observed in other β titanium alloys [25]. All gliding dislocations were found to have a/2 ⟨111⟩ Burger vectors that was determined by regular indexation method using the $\mathbf{g}\cdot\mathbf{b} = 0$ criterion. Similarly to previous investigations in β titanium alloys, screw segments of dislocations moved much slower than edge segments, leading to a large density of straight screw dislocations that ensure the deformation [11, 25, 26]. A typical example of the dislocation motion is shown in Fig. 6. Each micrograph from (a) to (d) was taken from a video recorded during an in situ experiment at several times noted on each image. These micrographs were taken using the diffraction vector $\mathbf{g} = [110]$ with a tilt angle of 13°. The corresponding stereographic projection of this grain is supplied in Fig. 6e with the poles and traces of interest. In order to determine the Burger vectors of dislocations visible on Fig. 6a–d, a micrograph of the same grain using another diffraction condition is shown in Fig. 6f with $\mathbf{g}' = [0\text{–}11]$: here, dislocations observed previously are invisible and only dislocations with another Burger vector are visible (it is also worth noting that these dislocations were invisible in previous micrographs). As glissile dislocations in β titanium alloys were only found to have a/2 ⟨111⟩ Burger vectors [11, 25, 26], present dislocations have thus a/2[111] Burger vector according to the notations used in Fig. 6e. An isolated dislocation, labeled with a black arrow in Fig. 6a, can be easily followed as an illustration of the typical motion of dislocations. The projection of its Burger vector is indicated in Fig. 6b by the letter "b," showing its screw character. Slip planes were determined from slip traces left by dislocations at the surfaces of the specimen (as the

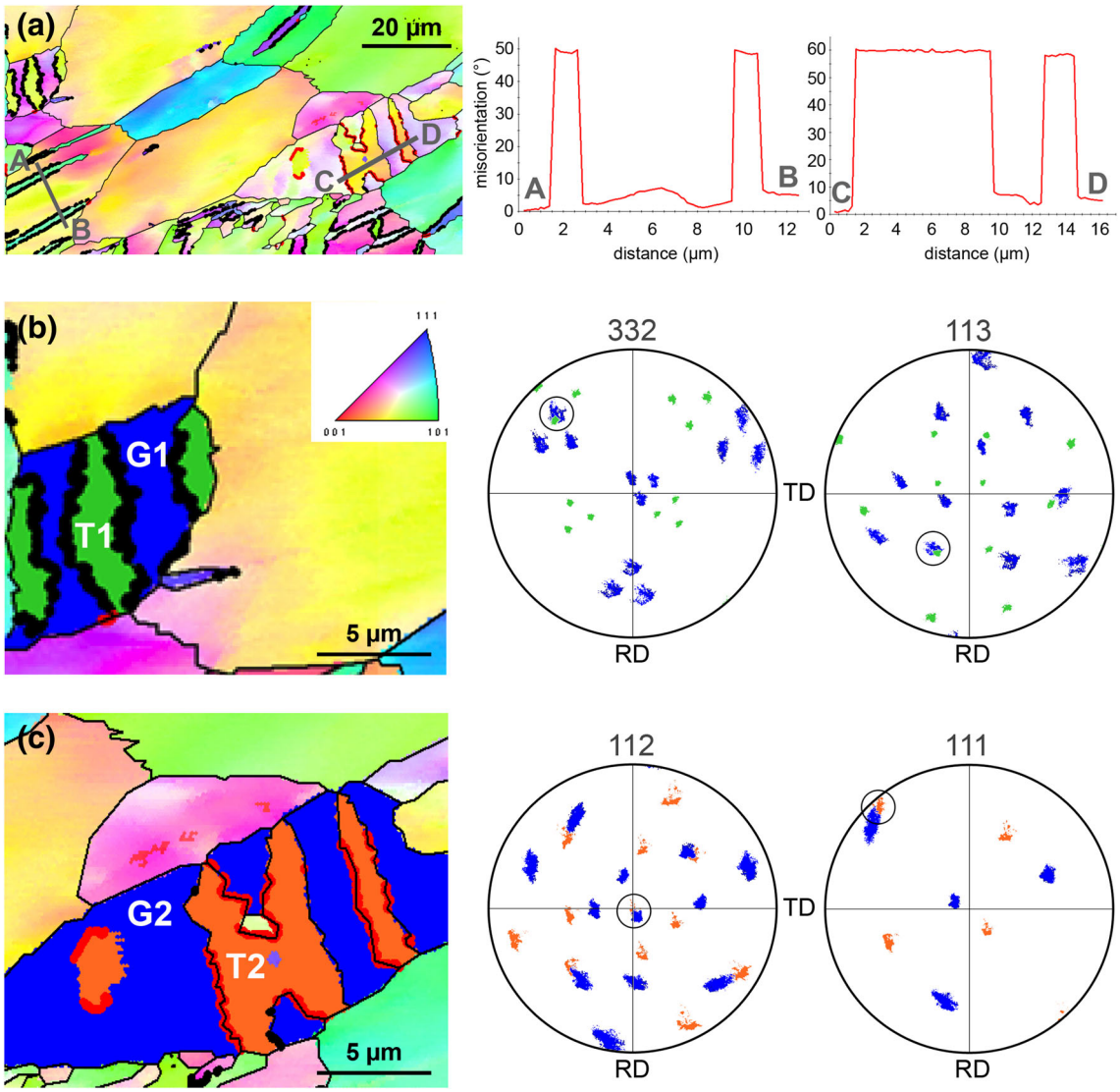


**Fig. 5** Inverse Pole Figure (IPF) EBSD cartographies from the Ti–23Nb–0.7Ta–2Zr–0.5N alloy after being deformed: **a** general cartography with two misorientation profiles along *AB* and *BC lines*; **b**, **c** zoomed cartographies with corresponding pole figures showing the twinning relationship between *G1* and *T1*, and *G2* and *T2*, respectively (*colors* of grains and twins do not correspond to crystallographic orientation here) (Color figure online)

"trace" labeled in Fig. 6d). In order to determine the slip plane, the angle of the slip trace was measured to be about 8° from the horizontal direction of the micrograph and compared to the stereographic projection in Fig. 6e. As possible slip planes in bcc metals are known to be {110}, {112} or, less frequently, {123} planes, only poles of these types of planes are indicated on the stereographic projection for a/2[111] Burger vector's dislocations. {110} poles are indicated by blue spots, {112} poles by green spots and {123} poles by black spots (see color online). Regarding the orientation of the slip trace, only (−312), (−211) or (−321) planes seem potential slip planes. The surface plane of the thin foil was also indexed as (−9 14 20) and its trace was drawn in dark gray as well as the traces of former planes in dark for the (−211) plane and in light gray for both potential {123} planes. Analysis of intersections between possible slip planes and the foil surface shown thus unambiguously that a/2[111] dislocations are gliding in the (−211) plane. Similarly, dislocations visible in

**Fig. 6** Sequence of images taken from a video recorded during an in situ straining experiment. A screw dislocation (*black arrow*) can be followed in **a**. A *white arrow* in **b** and **c** shows a loop left from double cross-slip. In **d**, the *white arrow* shows the point where the initial dislocation has left the previous loop behind. The corresponding stereographic projection is given in **e** and a micrograph of the same grain under a different diffraction condition is provided in **f** where the previous dislocations are invisible (Color figure online)

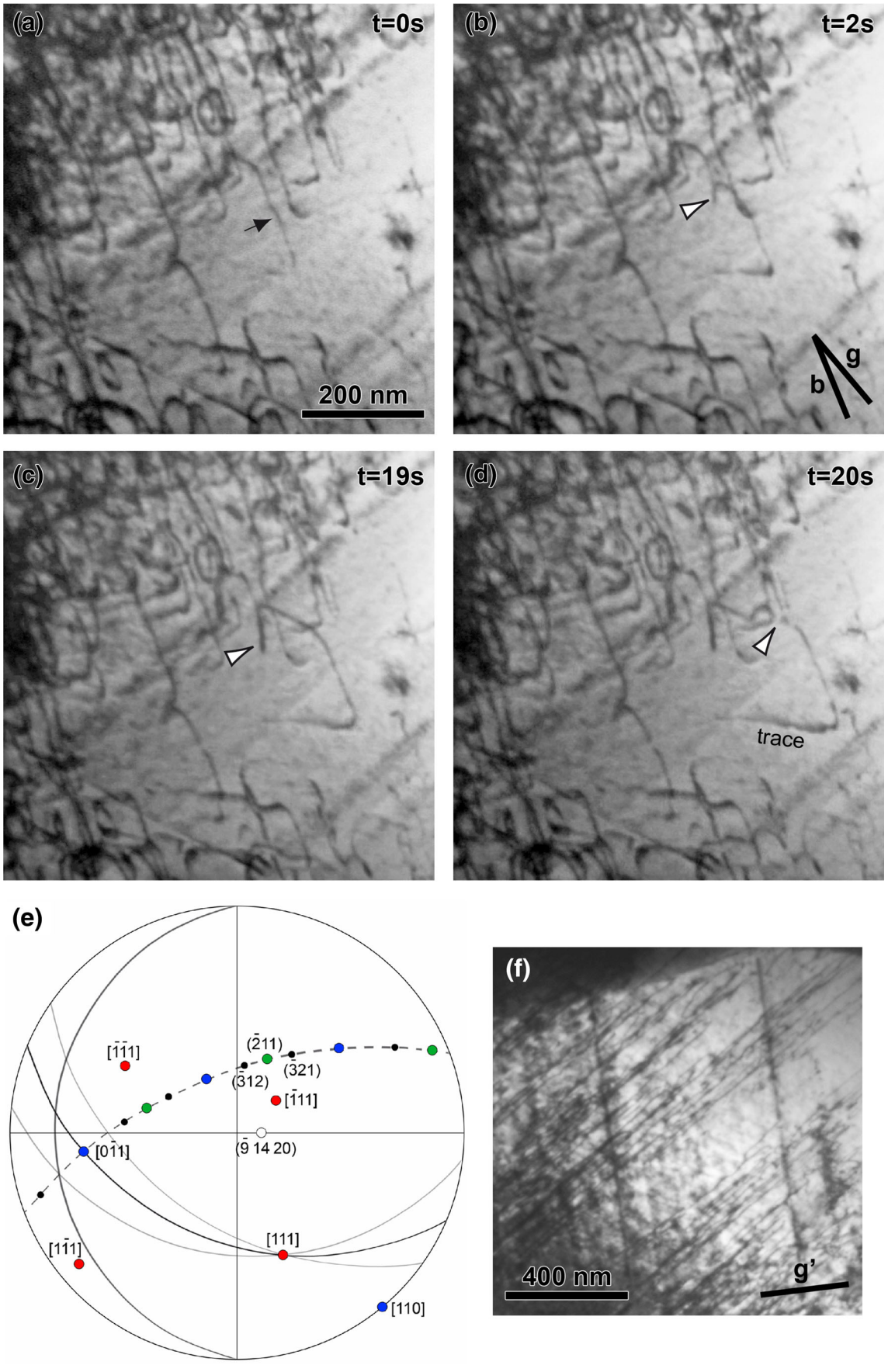
(a)
t=0s
200 nm
(b)
t=2s
g
b
(c)
t=19s
(d)
t=20s
trace
(e)
[1$\bar{1}\bar{1}$]
($\bar{2}$11)
($\bar{3}$21)
($\bar{3}$12)
[$\bar{1}$11]
[01$\bar{1}$]
($\bar{9}$ 14 20)
[111]
[11$\bar{1}$]
[110]
(f)
400 nm
g'

Fig. 6f were observed to glide in the (110) plane with a a/2[−111] Burger vector. Therefore, {112} and {110} slip planes were observed in accordance with slip systems commonly observed in bcc metals. The motion of the dislocation in Fig. 6 is typical of dislocations in β titanium alloys and bcc metals at low temperature [11, 25, 26]: the screw dislocation moves keeping straight and is subject to double cross-slip leading to multiplication. The white arrow in Fig. 6b and c shows a dislocation loop created by such phenomenon and still connected to the initial dislocation; on Fig. 6d, the white arrow indicates the point where the initial dislocation is separated from the created loop. The loop can next expand and contribute to the deformation of the material. This multiplication process involving double cross-slip as well as the main presence of straight screw dislocations is characteristic of the three-dimensionally spread core structure of screw dislocations that is assumed to be the key feature controlling the mobility of dislocations in bcc metals and thus in β titanium alloys [11, 25, 26].

According to the tensile curve presented in Fig. 3, large plastic deformation is obtained with the Ti–23Nb–0.7Ta–2Zr–0.5N alloy since almost 25 % of elongation at rupture can be reached. By comparison, the Ti–6Al–4V titanium alloy currently used for biomedical applications processes a maximum elongation at rupture situated at around 15 % of deformation. This large ductility is an interesting result because the presence of interstitial elements such as oxygen or nitrogen is well known to induce brittleness in titanium-based alloys. The reason of such ductility can be explained by the fact that additionally to dislocation glide, a massive twinning was also observed to accommodate the deformation. Such massive twinning provides effective obstacles to dislocations motion as it is the case for the well-known TWIP steels [27]. It is worth noting that we have observed a similar behavior in a recent work carried out in a highly deformable Ti–Mo metastable β-alloy in which a new transformation induced plasticity (TRIP)–twinning induced plasticity (TWIP) mechanism was highlighted [28].

## Electrochemical and Corrosion Behavior

From the cyclic potentiodynamic polarization experiments, the main electrochemical parameters obtained for the superelastic Ti–23Nb–0.7Ta–2Zr–0.5N alloy in comparison with CP-Ti are listed in Table 1.

It can be observed that $E_{corr}$ and $E_p$ values for the Ti–23Nb–0.7Ta–2Zr–0.5N alloy are about 70 and 50 mV more electropositive than those of CP-Ti denoting the enhancement of the corrosion resistance. On the other hand, $|E_{corr} - E_p|$ value for the Ti–23Nb–0.7Ta–2Zr–0.5N alloy is lower compared with CP-Ti, which means a stronger, more rapid and easier passivation.

The corrosion resistance was evaluated from Tafel representations and the main corrosion parameters obtained for both Ti–23Nb–0.7Ta–2Zr–0.5N alloy and CP-Ti are listed in Table 2.

It resulted that the values of the corrosion current density, $i_{corr}$, the corrosion rate, $V_{corr}$, and the ion release rate for the Ti–23Nb–0.7Ta–2Zr–0.5N alloy significantly decreased in comparison with those of CP-Ti. Thus, the Ti–23Nb–0.7Ta–2Zr–0.5N alloy demonstrates a very high corrosion resistance. On the other hand, the polarization resistance, $R_p$, of the Ti–23Nb–0.7Ta–2Zr–0.5N alloy increased by around 20 and the ion release is 30 times lower compared to CP-Ti. Consequently, the Ti–23Nb–0.7Ta–2Zr–0.5N alloy possesses a perfect chemical stability, which is due to the presence of the alloying elements. Indeed, the composition and the thickness of native passive film formed on the Ti–23Nb–0.7Ta–2Zr–0.5N alloy was analyzed by X-ray photoelectron microscope in a previous study [29]. It was detected a dense passive layer of about 6.5 nm composed of oxides and oxynitrides of the transition Ti, Nb, Zr, Ta metals that assured the alloy structural integrity and anticorrosion resistance. This result is in accordance with others biocorrosion studies carried out on similar Ti-based alloys [30–32].

## In Vitro Behavior of Human Osteoblasts

It has to be highlighted that very few studies addressed the in vitro biocompatibility of the superelastic Ni-free Ti-based alloys [21, 33–35] and there is no available literature on their in vivo osseointegration capacity. In a recent study [34], in vitro experiments with MC3T3-E1 preosteoblasts carried out on a novel superelastic Ti–19Zr–10Nb–1Fe alloy demonstrated almost similar extent of cell adhesion and proliferation on both the Ti–19Zr–10Nb–1Fe and NiTi alloys. In a previous study [35], the Ti–23Nb–0.7Ta–2Zr–

**Table 1** Main electrochemical parameters for CP-Ti and Ti–23Nb–0.7Ta–2Zr–0.5N alloy in Ringer solution at neutral pH and at 37 °C

| Material | $E_{corr}$ (mV) | $E_p$ (mV) | $\Delta E_p$ (mV) | $\lvert E_{corr} - E_p \rvert$ (mV) | $i_p$ (μA/cm$^2$) |
|---|---|---|---|---|---|
| CP-Ti | −320 | −200 | >1000 | 120 | 15.2 |
| Ti–23Nb–0.7Ta–2Zr–0.5N | −250 | −150 | >1000 | 100 | 2.3 |

**Table 2** Main corrosion parameters for CP-Ti and Ti–23Nb–0.7Ta–2Zr–0.5N alloy in Ringer solution at neutral pH and at 37 °C

| Material | $i_{corr}$ (μA/cm$^2$) | $V_{corr}$ (μm/Y) | Ion release (ng/cm$^2$) | $R_p$ (kΩ cm$^2$) |
|---|---|---|---|---|
| CP-Ti | 0.724 | 8.326 | 845.9 | 18.2 |
| Ti–23Nb–0.7Ta–2Zr–0.5N | 0.031 | 0.277 | 28.2 | 351.3 |

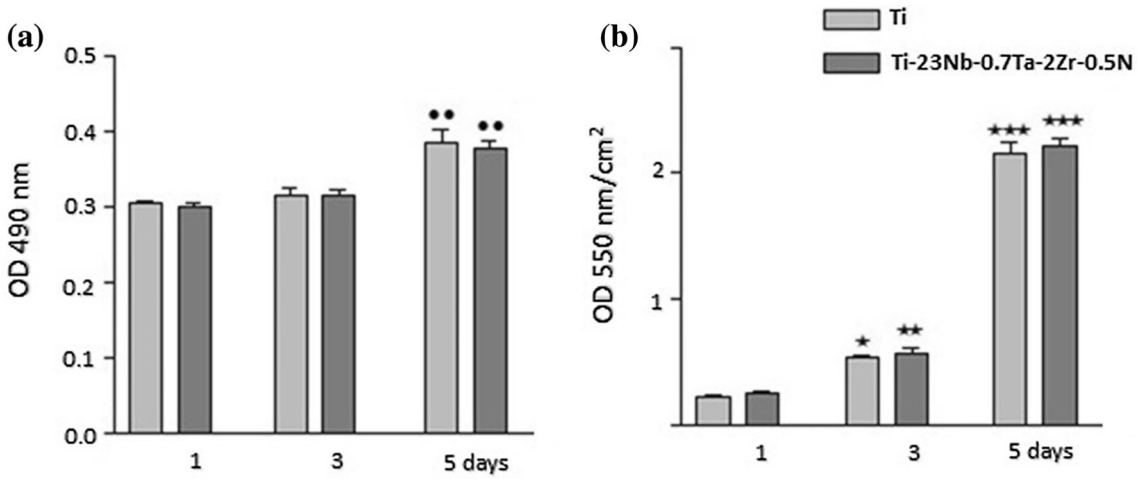


**Fig. 7** Viability of MG63 osteoblast-like cells cultured onto CP-Ti and Ti–23Nb–0.7Ta–2Zr–0.5N alloy for 1, 3, and 5 days as determined by **a** LDH and **b** MTT assays. Data analysis was based on mean ± SD ($n = 3$). ••$p < 0.01$ versus corresponding sample at 1 and 3 days; $^{\star}p < 0.05$ versus corresponding sample at 1 day; $^{\star\star}p < 0.01$ versus corresponding sample at 1 day; $^{\star\star\star}p < 0.001$ versus corresponding sample at 1 day

0.5N alloy was shown to support MC3T3-E1 pre-osteoblasts attachment, spreading and proliferation to a similar level with that displayed by the Ti–6Al–4V control sample. However, a substantial increase in the differentiation and mineralization ability of osteoblasts was observed for Ti–23Nb–0.7Ta–2Zr–0.5N substrate and no significant inflammatory response was elicited in macrophage cells cultured on this material. An important feature of any biomaterial for clinical applications is the lack of cytotoxicity. In order to determine the possible detrimental effects exerted by all biomaterials on the cell viability, the release of lactate dehydrogenase (LDH) into the culture media was quantified as an index of cell death. As it can be seen in Fig. 7a, MG63 cells exhibit a comparable viability on CP-Ti and Ti–23Nb–0.7Ta–2Zr–0.5N. Thus, the time-dependent profiles of LDH activity revealed no significant differences between the two analyzed substrates at any point in time. Moreover, LDH activity recorded approximately similar optical density (OD) values at 1 and 3 days after seeding. A higher activity but not a significant one for the loss of membrane integrity was remarked between the 3rd and 5th days of culture. This could be associated with the confluence initiated cell death. Consequently, both samples elicit no significant cytotoxic responses from MG63 osteoblasts and do not alter cell viability. Furthermore, the proliferation status of the total population of cells was assessed by MTT colorimetric method. As shown in Fig. 7b, the number of viable metabolically active osteoblasts on the analyzed substrates equally increased from the first to the 5th day of culture. By day 5, the proliferation rates on the two surfaces were significantly higher than those found after 1 and 3 days of culture. In a very recent study [29], we have observed on the Ti–23Nb–0.7Ta–2Zr–0.5N alloy the cell-to-substrate interaction by double fluorescent staining of vinculin and actin filaments. These observations have revealed the typical appearance of osteoblast cells with well-expressed stress fibers oriented parallel to one another and to the long axis of the cell and punctiform vinculin signals at the termini of actin microfilament bundles. On the other hand, no significant differences in terms of cell spreading, cytoskeleton organization, and focal contact formation could be observed between Ti–23Nb–0.7Ta–2Zr–0.5N and CP-Ti [29]. Taken together, these findings prove that the studied Ti–23Nb–0.7Ta–2Zr–0.5N alloy favors cell proliferation without showing any deleterious effect suggesting increased biocompatibility.

## Conclusion

In this study, the deformations mechanisms and the biocompatibility of a new superelastic Ti–23Nb–0.7Ta–2Zr–0.5N alloy composition were investigated.

By tensile tests, high tensile strength (700 MPa), low Young's modulus (50 GPa), and excellent ductility (25 % of elongation at rupture) were observed for this alloy. On the other hand, its superelastic behavior was evidenced by cyclic tensile tests, which is due to the reversible stress-induced $\alpha''$ martensitic transformation occurring. Consequently, a high elastic recovery of about 2.2 % was obtained demonstrating the good superelastic property of this alloy. The high tensile strength observed is due to the nitrogen addition, which is well known to involve a solid-solution hardening effect in alloys.

The plastic deformation of the present superelastic alloys was shown to be largely accommodated by twinning and the two $\{332\}\langle 113\rangle$ and $\{112\}\langle 111\rangle$ twinning systems were observed to be activated by EBSD. Dislocation activity also takes place during plastic deformation. The dislocation behavior was found to be similar to other metastable β titanium-based alloys with mainly a/2 $\langle 111\rangle$ screw dislocations gliding in {110} or {112} planes. Thus, the plastic deformation was shown to be accommodated by both dislocation glide and massive twinning which contribute to the high ductility observed.

Moreover, all electrochemical and corrosion parameters obtained in neutral Ringer solution showed that the Ti–23Nb–0.7Ta–2Zr–0.5N presents nobler electrochemical behavior and superior anticorrosive resistance in comparison with CP-Ti. On the other hand, cell culture experiments with MG63 osteoblast-like cell line proved that the studied alloy favor cell proliferation and the absence of any deleterious effect on cultured cells suggests increased biocompatibility.

Thus, all the characteristics observed for the superelastic Ti–23Nb–0.7Ta–2Zr–0.5N alloy make this material potentially very interesting for biomedical applications.

**Acknowledgments** This study was financially supported by the Romanian Ministry of National Education (Project PN-II-ID-20-RO-FR-2014) and by the French National Research Agency (Project ANR-13-IS09-0008-01). The authors also acknowledge financial support from the French CNRS and CEA METSA network for in situ TEM experiments.

## References

1. Wever DJ, Veldhuizen AG, Sanders MM, Schakenraad JM, Van Horn JR (1997) Cytotoxic, allergic and genotoxic activity of a nickel-titanium alloy. Biomaterials 18:1115–1120
2. Niinomi M (2003) Fatigue performance and cytotoxicity of low rigidity titanium alloy, Ti–29Nb–13Ta–4.6Zr. Biomaterials 24:2673–2683
3. Miyazaki S, Kim HY, Hosoda H (2006) Development and characterization of Ni-free Ti-base shape memory and superelastic alloys. Mater Sci Eng A438–440:18–24
4. Laheurte P, Prima F, Eberhardt A, Gloriant T, Wary M, Patoor E (2010) Mechanical properties of low modulus β titanium alloys designed from the electronic approach. J Mech Behav Biomed Mater 3:565–573
5. Kim HY, Ikehara Y, Kim JI, Hosoda H, Miyazaki S (2006) Martensitic transformation, shape memory effect and superelasticity of Ti–Nb binary alloys. Acta Mater 54:2419–2429
6. Bertrand E, Castany P, Gloriant T (2013) Investigation of the martensitic transformation and the damping behavior of a superelastic Ti–Ta–Nb alloy. Acta Mater 61:511–518
7. Huiskes R, Weinans H, Van Rietbergen B (1992) The relationship between stress shielding and bone resorption around total hip stems and the effects of flexible materials. Clin Orthop Relat Res 274:124–134
8. Fukui Y, Inamura T, Hosoda H, Wakashima K, Miyazaki S (2004) Mechanical properties of a Ti–Nb–Al shape memory alloy. Mater Trans 45:1077–1082
9. Hao YL, Zhang ZB, Li SJ, Yang R (2012) Microstructure and mechanical behavior of a Ti–24Nb–4Zr–8Sn alloy processed by warm swaging and warm rolling. Acta Mater 60:2169–2177
10. Tahara M, Kim HY, Hosoda H, Nam TH, Miyazaki S (2010) Effect of nitrogen addition and annealing temperature on superelastic properties of Ti–Nb–Zr–Ta alloys. Mater Sci Eng A527:6844–6852
11. Besse M, Castany P, Gloriant T (2011) Mechanisms of deformation in Gum Metal TNTZ-O and TNTZ titanium alloys: a comparative study on the oxygen influence. Acta Mater 59:5982–5988
12. Ramarolahy A, Castany P, Prima F, Laheurte P, Peron I, Gloriant T (2012) Microstructure and mechanical behavior of superelastic Ti–24Nb–0.5O and Ti–24Nb–0.5N biomedical alloys. J Mech Behav Biomed Mater 9:83–90
13. Saito T, Furuta T, Hwang JH, Kuramoto S, Nishino K, Suzuki N, Chen R, Yamada A, Ito K, Seno Y, Nonaka T, Ikehata H, Nagasako N, Iwamoto C, Ikuhara Y, Sakuma T (2003) Multifunctional alloys obtained via a dislocation-free plastic deformation mechanism. Science 300:464–467
14. Hanada S, Izumi O (1986) Transmission electron-microscopic observations of mechanical twinning in metastable beta titanium alloys. Metall Trans A 17:1409–1420
15. Furuhara T, Nakamori H, Maki T (1992) Crystallography of alpha precipitated on dislocations and deformation twin boundaries in a beta titanium alloy. Mater Trans JIM 33:585–595
16. Bertrand E, Castany P, Péron I, Gloriant T (2011) Twinning system selection in a metastable beta-titanium alloy by Schmid factor analysis. Scr Mater 64:1110–1113
17. Cai Z, Nakajima H, Woldu M, Berglund A, Bergman M, Okabe T (1999) In vitro corrosion resistance of titanium made using different fabrication methods. Biomaterials 20:183–190
18. Gordin DM, Gloriant T, Chane-Pane V, Busardo D, Mitran V, Hoche D, Vasilescu C, Drob SI, Cimpean A (2012) Surface characterization and biocompatibility of titanium alloys implanted with nitrogen by Hardion + technology. J Mater Sci 23:2953–2966
19. Calderon-Moreno JM, Vasilescu E, Drob P, Osiceanu P, Vasilescu C, Drob SI, Popa M (2013) Surface and electrochemical characterization of a new ternary titanium based alloy behaviour in electrolytes of varying pH. Corros Sci 77:52–63
20. Gordin DM, Ion R, Vasilescu C, Drob SI, Cimpean A, Gloriant T (2014) Potentiality of the 'Gum Metal' titanium based alloy for biomedical applications. Mater Sci Eng C 44:362–370
21. Cimpean A, Mitran V, Ciofrangeanu CM, Galateanu B, Bertrand E, Gordin DM, Iordachescu D, Gloriant T (2012) Osteoblast cell behavior on the new beta-type Ti-25Ta-25 Nb alloy. Mater Sci Eng C 32:1554–1563
22. Morniroli JP, Gantois M (1973) Study of conditions under which omega-phase forms in titanium-niobium and titanium-molybdenum alloys. Mem Sci Rev Metall 70:831–842

23. Tang X, Ahmed T, Rack HJ (2000) Phase transformations in Ti-Nb-Ta and Ti-Nb-Ta-Zr alloys. J Mater Sci 35:1805–1811
24. Ping DH, Cui CY, Yin FX, Yamabe-Mitarai Y (2006) TEM investigations on martensite in a Ti-Nb-based shape memory alloy. Scr Mater 54:1305–1310
25. Castany P, Besse M, Gloriant T (2011) Dislocation mobility in gum metal β-titanium alloy studied via in situ transmission electron microscopy. Phys Rev B 84:020201
26. Castany P, Besse M, Gloriant T (2012) In situ TEM study of dislocation slip in a metastable β titanium alloy. Scr Mater 66:371–373
27. Grässel O, Krüger L, Frommeyer G, Meyer LW (2000) High strength Fe-Mn-(Al, Si) TRIP/TWIP steels development-properties-application. Int J Plast 16:1391–1409
28. Sun F, Zhang JY, Marteleur M, Gloriant T, Vermaut P, Laillé D, Castany P, Curfs C, Jacques PJ, Prima F (2013) Investigation of early stage deformation mechanisms in a metastable β titanium alloy showing combined twinning-induced plasticity and transformation-induced plasticity effects. Acta Mater 61:6406–6417
29. Mitran V, Vasilescu C, Drob SI, Osiceanu P, Calderon-Moreno JM, Tabirca MC, Gordin DM, Gloriant T, Cimpean A (2015) Biological behaviour and enhanced anticorrosive performance of the nitrided superelastic Ti-23Nb-0.7Ta-2Zr-0.5N alloy. Biomed Res Int 2015:ID 261802
30. Tanaka Y, Nakai M, Akahori T, Niinomi M, Tsutsumi Y (2008) Doi H, Hanawa T Characterization of air-formed surface oxide film on Ti–29Nb–13Ta–4.6Zr alloy surface using XPS and AES. Corros Sci 50:2111–2116
31. Okazaki Y, Rao S, Ito Y, Tateishi T (1998) Corrosion resistance, mechanical properties, corrosion fatigue strength and cytocompatibility of new Ti alloys without Al and V. Biomaterials 19:1197–1215
32. Mareci D, Chelariu R, Gordin DM, Ungureanu G, Gloriant T (2009) Comparative corrosion study of Ti–Ta alloys for dental applications. Acta Biomater 5:3625–3629
33. Park CH, Lee CS, Kim YJ, Jang JH, Suh JY, Park JW (2011) Improved pre-osteoblast response and mechanical compatibility of ultrafine-grained Ti-13Nb-13Zr alloy. Clin Oral Impl Res 22:735–742
34. Xue P, Li Y, Li K, Zhang D, Zhou C (2015) Superelasticity, corrosion resistance and biocompatibility of the Ti-19Zr-10Nb-1Fe alloy. Mater Sci Eng C50:179–186
35. Ion R, Gordin DM, Mitran V, Osiceanu P, Dinescu S, Gloriant T, Cimpean A (2014) In vitro bio-functional performances of the novel superelastic beta-type Ti–23Nb–0.7Ta–2Zr–0.5N alloy. Mater Sci Eng C 35:411–419